Spectral Analysis for Resonant Soft X-Ray Scattering Enables Measurement of Interfacial Width in 3D Organic Nanostructures

Thomas Ferron, Michael Pope, and Brian A. Collins*
Department of Physics and Astronomy, Washington State University, Pullman, Washington 99164, USA
(Received 2 June 2017; revised manuscript received 1 August 2017; published 19 October 2017)

Interfaces are of critical importance to many materials and phenomena yet are difficult to probe. This difficulty is compounded in three-dimensional nanostructures and with delicate organic materials. Here we demonstrate a quantitative spectral analysis of resonant soft x-ray scattering that can accurately measure properties of buried nonplanar interfaces within polymeric systems. We measure the scattering invariant on an absolute scale to quantify the interfacial volume and width involved in mixing at the interface of block copolymer nanostructures. Using continuous contrast tuning, this spectral analysis enables the separation and identification of any number of unique scatterers in complex nanostructures.

DOI: 10.1103/PhysRevLett.119.167801

Emergent phenomena and properties within materials and devices often originate at interfaces [1–4]. Thus, tools to study interfacial structure are of high importance but are rare, especially for organic or biological nanostructured devices or tissues that contain delicate, low-contrast, and nonplanar interfaces. Block copolymers (BCP) represent a good example of such materials. BCPs are molecules that consist of unique polymer segments connected through covalent bonds at the chain end and can thermodynamically phase separate into ordered three-dimensional bulk nanostructures [5]. They are of particular interest for sub-10 nm photolithography [6,7] or bottom-up assembly of functional nanomaterials and devices [8–10]. Applications require a detailed understanding of the interfaces because sharpness and ordering of these interfaces determine the limiting size of nanostructures [6] as well as optical or electronic coupling and interfacial states between the blocks [10,11]. Thus, interfacial width is a valuable parameter in optimizing BCP nanostructures.

Historically, methods employed to measure the nanometer-scale lateral structure and interfacial width include small angle scattering (SAS, via x rays or neutrons, for example), dynamic secondary ion mass spectrometry (SIMS), and specular reflectivity. SAS experiments have attempted to utilize Porod's law at high scattering angles. However, limitations from low-contrast and error-prone background subtractions make a determination of the interfacial width challenging [12]. SIMS measurements, on the other hand, are limited by low spatial resolution [13]. Instead, neutron specular reflectivity of polymer layers has been more successful, where a component is isotopically labeled in order to increase contrast. However, isotopic labeling can lead to alteration of interfacial parameters [14]. Specular reflectivity measurements are, furthermore, incapable of measuring lateral structures key in burgeoning technologies based on BCP materials.

Recent utilization of resonant soft x rays at elemental absorption edges has begun to alleviate some difficulties presented in standard x-ray or neutron techniques [15–17]. Near an elemental absorption edge, a molecule's complex index of refraction $n(E) = 1 - \delta(E) + i\beta(E)$ fluctuates as a function of energy due to resonances involving electronic transitions from core atomic states to unoccupied molecular orbitals. Varying the photon energy effectively tunes molecular contrast, similar to isotopic labeling in neutron experiments, except resonant contrast is intrinsic to the molecule and tunable on a single sample.

To date, resonant soft x-ray scattering (RSOXS) has primarily been used in soft matter characterization to enhance scattering signal [16,18–20]. Quantitative spectral analyses and contrast tuning [21,22] have lagged inorganic systems [23–25] due to the complex nature of the molecular absorption fine structure. RSOXS allows for the chemical determination of scattering sources through spectral modeling because this fine structure encodes the chemical fingerprint of each molecule [22]. Sensitivity to transition dipole moments additionally enables correlative local measurements of molecular orientation [26–28]. To quantify these measurements, including BCP interfacial width, absolute scattering intensity is required. Unfortunately, while absolute SAS calibration standards have become increasingly available [29], the low penetration depth of soft x rays renders these resources unusable at absorption edges. Thus, independent experimental methods must be developed before quantitative measurements of these critical BCP interface phenomena can be realized.

In this Letter we demonstrate both a quantitative spectral model for scattering across an absorption edge and a facile method to measure absolute scattering intensity that takes advantage of the historically undesirable x-ray fluorescence (XRF) background signal. This method enables measurement of potentially unlimited numbers of chemically independent molecular species in a composite nanostructure thin film. Through quantitative analysis of the scattering invariant, we extract both material phase and interface information of assembled three-dimensional nanostructures

of a model BCP, thus enabling high-precision measurements of nanostructure in soft matter.

The scattering invariant Q is defined as the overall scattering power of the sample and only depends on the mean square fluctuations, Δn. The invariant is so named because it does not depend on how those fluctuations are distributed in space (i.e., size of the structure); however, it does assume sharp interfaces between scatterers [30]. Mixing at these interfaces reduces the mean square fluctuation, and therefore Q is sensitive to interfacial mixing if measured on an absolute scale. The scattering power is experimentally determined through an integral of scattering intensities $I(\boldsymbol{q}, E)$ over three-dimensional reciprocal space $\boldsymbol{q}$ (the momentum transfer wave vector E is the photon energy). Since experimental measurements are constrained to a finite region in $\boldsymbol{q}$, we refer to these measurements as the total scattering intensity (TSI). In contrast, Q can be calculated by modeling an arbitrary number of domains contributing to scattering in a multidomain model adopted from Tatchev [31]. If we assume p domains separated by a discrete boundary

$$Q(E) = \frac{4\pi^2 V E^4}{(hc)^4} \sum_{i,j=1}^{p-1} \Delta n_{ip}(E) \Delta n^*_{jp}(E) \tilde{Q}_{ij}, \qquad (1)$$

where h is Planck's constant, c is the speed of light, V is the illuminated volume, Δn_{ij} is the difference in index of refraction between domains i and j, and $\tilde{Q}_{ij}$ is the partial invariant between those domains, which originates from the autocorrelation function or pair correlation function for diagonal terms and off diagonal terms, respectively. Equation (1) can be reduced to traditional two-phase expressions [30] by setting $p = 2$, and identifying $\tilde{Q}_{ij}$ as the product of volume fractions between domains i and j. This model enables one to separately incorporate scattering from multiple components. If the optical constants (index) are known for each component, then the scattering from each can be separately isolated, simplifying analysis.

In order to demonstrate the above model we investigated BCP poly(styrene-block-methyl methacrylate) (PS-b-PMMA) thin films of varying molecular weights, targeting specific internal nanostructures based on the molar ratio between components (lamellar, hexagonal close packed cylinders, and base-center cubic spheres—see Supplemental Material [32] for details of samples and their preparation) [5]. Additionally, both blocks being coil-like, there is negligible x-ray dichroism or birefringence, allowing us to use scalar optical constants. This is important since molecular orientational correlations within nanostructures can occur with rodlike molecules, resulting in anisotropic scattering patterns that could complicate analysis [26].

Component optical constants shown in Fig. 1(a) were calculated by Yan *et al.* via near edge x-ray absorption fine structure spectroscopy measurements on pure films of the polymer components [33]. Isolating unique molecular species experimentally is facile for synthetic molecules, and incorporating additional chemistry and orientation through calculations is improving dramatically [34,35]. In this study, three domains were taken into consideration: PS, PMMA, and vacuum. Vacuum is included here to incorporate scattering from surface roughness that is often the source of background that interferes with quantifying scattering signals. Therefore, the three contrast functions in Fig. 1(b) represent the possible sources of scattering signal. Each function exhibits a unique, rapidly changing signal as a function of energy. Over the carbon edge, scattering contrast from these pairs varies by 4 orders of magnitude. Such a dramatic fluctuation arises from the fine structure in the optical constants and makes this technique particularly sensitive to multiple types of scatterers—allowing massive contrast enhancement at one energy and perfect contrast nulling at another. This variation is superior to deuteration for neutron scattering and eliminates the necessity of multiple, chemically altered samples.

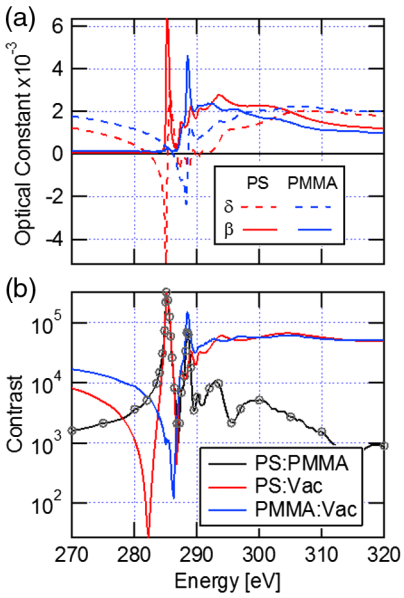

FIG. 1. (a) Complex optical constants for PS and PMMA. (b) Contrast functions $C = E^4 \Delta n^2_{\mathrm{AB}}$ for three modeled domains: PS, PMMA, and vacuum (arising from surface roughness). Circles indicate photon energies where RSOXS was measured.

Resonant scattering in transmission geometry was completed at beam line 11.0.1.2 at the Advanced Light Source with detailed procedures previously reported [36]. Scattered energies utilized are indicated in Fig. 1(b). Lacking a soft x-ray calibration standard, we determine absolute scattering calibration through measurement of the 277 eV XRF background. Without energy discrimination in our detector, the measured signal I_m integrates both scattering and isotropic XRF

$$I_m(\boldsymbol{q}, E) = R_r[I_{\mathrm{scat}}(\boldsymbol{q}, E) \cdot T(E) + I_{\mathrm{XRF}}(E)], \qquad (2)$$

where R_r is the relative responsivity between the GaAs photodiode and Princeton Instruments MTE CCD detector

used to measure the incident and outgoing photon intensity, respectively. Transmittance through the sample $T(E)$ is measured directly at the location of scattering by the photodiode with and without the sample. Fluorescence intensity is calculated by the tabulated quantum yield of the carbon K_α transition ($\omega_{C_{K\alpha}} = 0.002575$) [37] and the number of absorbed photons (Fig. S2) $I_{\mathrm{XRF}}(E) = \omega_{C_{K\alpha}}[1 - T(E)]/4\pi$. The measured I_{XRF} is extracted as a constant background from I_m by fitting film scattering at high q to a power law simultaneously at two separate energies—one above and one below the absorption edge (Fig. S3). Comparing the measured and calculated XRF reveals the relative responsivity R_r between the detectors, enabling calibration of absolute scattering intensity to within 8% uncertainty, currently limited by beam stability.

RSOXS data for one sample across the carbon absorption edge are shown in Fig. 2, which reveals significant structure as a function of both q and E. Select lineouts are shown in Fig. 2(b) normalized to the primary BCP scattering peak at $q^* = 0.094\ \mathrm{nm}^{-1}$, corresponding to a long period $L = 66.8$ nm. Secondary peaks at $2q^*$ and $3q^*$ indicate the presence of lamellar nanostructure as predicted by the phase diagram for this sample. Interestingly, these profiles deviate from each other outside the primary peak, at both low and high q. Profiles measured at a photon energy corresponding to the $\pi^*_{C=C}$ transition for PS (285.1 eV) are qualitatively the most consistent with ideal BCP scattering as this is where the contrast function between PS and PMMA is maximized. In contrast, scattering from roughness dominates low-q regions and at energies both below and above the edge [Fig. 2(a)]. Fluorescence additionally dominates the high-q data above the edge [Fig. 2(a)]. TSI(E) is given in Fig. 2(c) and exhibits a rapidly changing signal. In fact, TSI(E) near 286 eV fluctuates by more than 2 orders of magnitude over ± 1 eV, consistent with the contrast functions in Fig. 1(b).

Experimental measurement of the invariant has historically been accomplished by assuming isotropic scattering and is commonly used to measure the domain purity in polymer blend thin films [19,38,39]. As a consequence, vertical structure is ignored by considering only in-plane scattering in the traditional transmission geometry. In many cases thin films whose thickness is on the size scale of morphological features will have significantly different structure vertically versus in the film plane, resulting in cylindrical rather than spherical scattering symmetry. The required information could be obtained through a grazing incidence measurement. However, complex scattering models beyond the Born approximation [40,41] are required to quantitatively interpret such data. Instead we retain the simplicity of transmission geometry by rotating the film from normal incidence to 20° as shown in Fig. 3(a). Rotating the sample will express the scattering component (q_z) perpendicular to the substrate and is shown for two samples in Fig. 3(b) along with atomic force microscopy

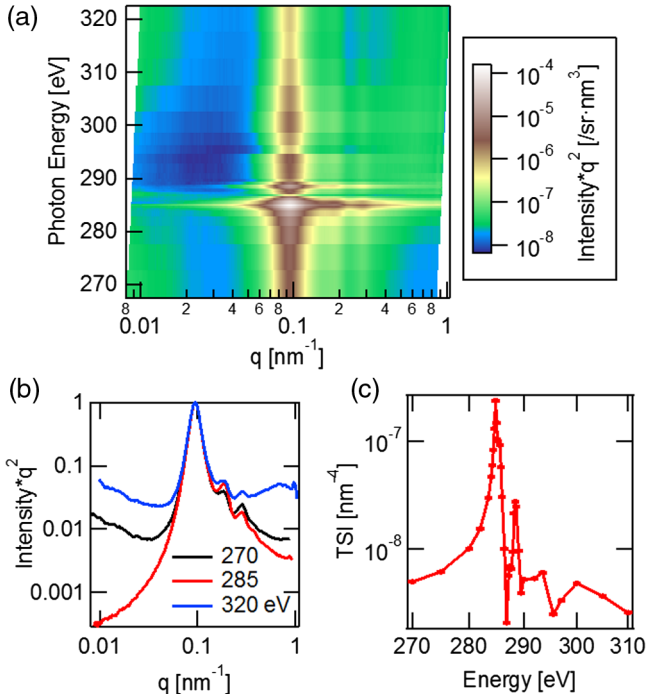

FIG. 2. (a) Scattering intensity ($*q^2$ to accentuate features) as a function of both $|\mathbf{q}|$ and E. (b) Individual scattering profiles at select energies normalized to the BCP q^* peak. (c) Total scattering intensity as a function of energy.

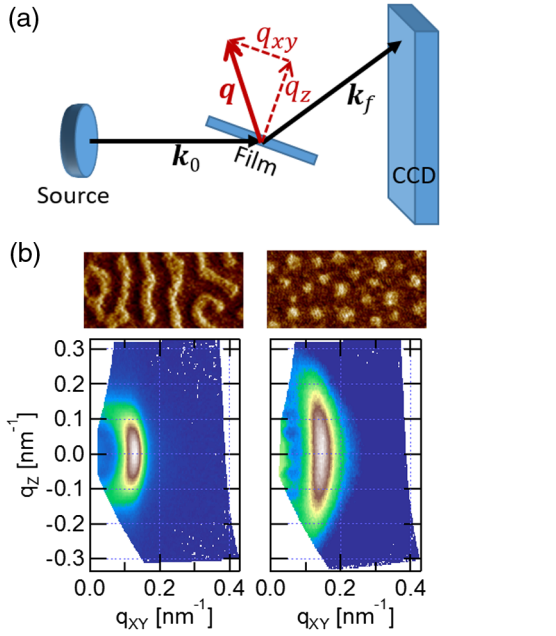

FIG. 3. (a) Transmission scattering geometry enabling measurement of reciprocal space maps with one CCD exposure. k_0, k_f are the incident and scattered wave vectors, respectively. (b) Atomic force microscopy phase images and corresponding reciprocal space maps ($E = 285.1$ eV) of a lamellar (left) and hexagonal close packed cylinder (right) BCP nanostructure.

(AFM) of their lateral morphology. The scattering data demonstrate the elliptical patterns, which vary qualitatively by sample and thus must be measured directly. We correct our measured TSI through a ratio of the invariant calculated through cylindrical and spherical integration. Correction factors for all samples are given in Table S1 and often require a $\pm 20\%$ correction, suggesting that previous analyses of TSI for domain composition might contain errors on this level [19,38,39].

By integrating Eq. (2) over $\boldsymbol{q}$, I_{scat} becomes Q and can be combined with Eq. (1). We fit the measured TSI(E) to this combined model, which contains only the four $\tilde{Q}_{ij}$ parameters plus an energy offset between the measured optical constants and the TSI data. The diagonal invariants represent material scattering between styrene and methacrylate domains $\tilde{Q}_{\mathrm{SM}}$ and vacuum scattering from surface roughness $\tilde{Q}_{\mathrm{vac}}$, while the off diagonals represent cross correlations between the two. Simultaneous fitting over all samples is conducted to ensure an identical relative energy calibration. An example fit is illustrated in Fig. 4 with all results shown in Fig. S5. The only inputs to the model are the optical constants displayed in Fig. 1 and the measured $T(E)$. Figure 4 also displays each source contribution resulting in the full model. Material scattering is responsible for approximately 90% of the total signal at lower energies. Above 290 eV, XRF and vacuum scattering (surface roughness) begin to contribute ~50% the signal making separate quantification important in analysis.

Interestingly, $\tilde{Q}_{\mathrm{vac}} \cong 0.01\tilde{Q}_{\mathrm{SM}}$. This agrees with the relative volume of the surface region compared with the bulk where AFM measures a rms roughness averaging about 1% of the total thickness. Using this relationship and tabulated atomic scattering factors [42], we calculate the expected scattering from surface roughness to make up 60% of the total signal using hard x rays at 10 keV. Without precise methods to disentangle these two sources of scattering, accurate absolute measurement of domain scattering becomes impossible.

$\tilde{Q}_{\mathrm{SM}}$ equals the product of volume fractions for the two components assuming sharp interfaces and is plotted as the red line in Fig. 5(a) as a function of the known volume fraction of PMMA (ϕ_M). Qualitatively, the extracted values follow the expected trend. However, the measurements are systematically lower than predicted. This is because entropic mixing of the two polymer components at the BCP interfaces reduces the mean squared fluctuation within the sample and therefore the measured scattering. This reduction originates from an effective volume or interphase region that does not contribute to the scattering. The composition across the interface can be modeled as an error function and the effective interphase can be subtracted from the scattering volume using $\tilde{Q}_{\mathrm{SM}} = \phi_S\phi_M - (\sqrt{2}/2\pi)(S/V)W$ [30], where S is the total area of the interface, V is the sample volume, and W is the interfacial width. If we assume a perfectly constructed lattice following the BCP phase diagram, we can calculate S/V for each morphology leaving only W as an unknown parameter. Figure 5(b) gives the resulting interfacial width measurement with an average of $W = 4.4 \pm 0.7$ nm. This is slightly lower than the width for these materials measured with reflectivity (5.0 nm) [15] yet agrees within the uncertainty. The error bars are dominated by poor beam

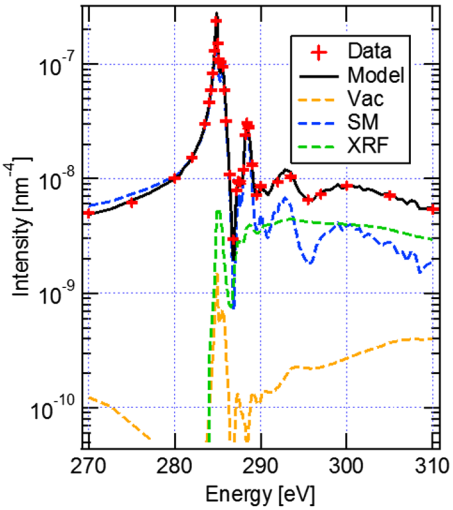

FIG. 4. Example fit of the TSI data to the combined Eqs. (1) and (2). Dashed are terms in the sum for the combined model defined in the text. Uncertainties are derived from detector statistics for scattering and optical constants.

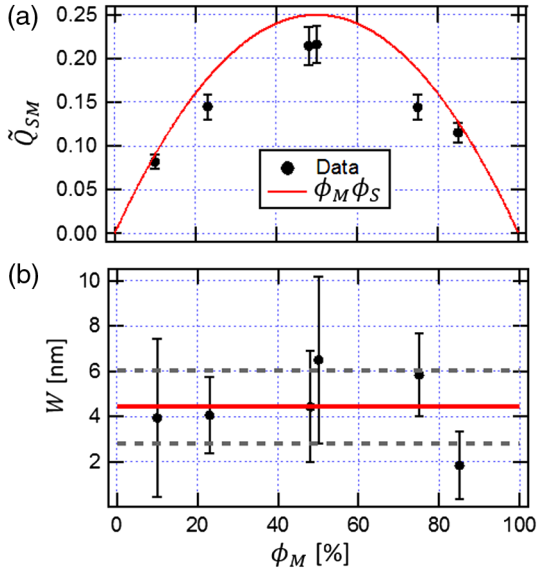

FIG. 5. (a) Partial invariant corresponding to domain scattering plotted against sample PMMA volume fraction ϕ_M. Data (black circles) compared to calculation (line) assuming sharp interfaces. (b) Calculated interfacial width modeled as an error function. Average value (line) and standard deviation (dash) are shown. Uncertainties are propagated from fit results and absolute scattering calibration.

stability reported previously [28]. Significantly higher precision could be achieved with improvements of the beam line and in beam lines currently under construction.

This measurement is remarkable, first because the spectral model we use isolates domain scattering cleanly from other sources such as roughness scattering, absorption, and fluorescence effects. As there are no constraints on p in Eq. (1), this method could easily be expanded to systems containing an arbitrary number of unique molecular species in ordered structures and is free of the need for laborious and potentially disruptive labeling techniques. Without the intrinsic contrast variation at the absorption edge, this measurement is nearly impossible. In this application, we furthermore demonstrate quantitative measurement of a nonplanar interface, which is impossible with specular reflectivity—the only other successful direct measurement of interfacial width. In fact, reflectivity convolutes interfacial width with capillary fluctuations of the position of the interface. Our method removes this limitation and the narrower width we measure may actually be closer to the intrinsic interfacial width for this system. Although our polymers are well classified in the strong segregation limit [6], with improved precision this method could additionally contribute to thermodynamic investigation below this limit. Conversely, if W is known, the specific area S/V of the interface is accessible as well. Putting these advantages together, our method is well suited for future investigations into sub-10 nm patterning or functional nanostructures and devices [6–10].

In conclusion, we have employed a novel absolute scattering calibration and multidomain spectral model for RSOXS to determine the interfacial width of three-dimensional polymer nanostructures. The model identifies and isolates the sources of resonant scattering over the carbon K_α absorption edge enabling high-precision measurements. We show that over a range of BCP nanostructures the measured interfacial width agrees with previous measurements on planar structures. Our study allows for the direct measurement of interface properties in an assembled three-dimensional nanostructure, and with appropriately quantified optical constants, this application can extend to any elemental absorption edge or molecular material.

Dean Delongchamp, Daniel Sunday, and Wen-Li Wu are gratefully acknowledged for their discussions regarding the intersection of polymer physics and scattering. T. F. acknowledges support from the Washington State University Seed Grant for this work. This research used resources of the Advanced Light Source, which is a DOE Office of Science User Facility under Contract No. DE-AC02-05CH11231.

*brian.collins@wsu.edu

[1] A. Soumyanarayanan, N. Reyren, A. Fert, and C. Panagopoulos, Emergent phenomena induced by spin-orbit coupling at surfaces and interfaces, Nature (London) **539**, 509 (2016).

[2] K. Vandewal, S. Albrecht, E. T. Hoke, K. R. Graham, J. Widmer, J. D. Douglas, M. Schubert, W. R. Mateker, J. T. Bloking, G. F. Burkhard, A. Sellinger, J. M. J. Frechet, A. Amassian, M. K. Riede, M. D. McGehee, D. Neher, and A. Salleo, Efficient charge generation by relaxed charge-transfer states at organic interfaces, Nat. Mater. **13**, 63 (2014).

[3] A. E. Jailaubekov, A. P. Willard, J. R. Tritsch, W.-L. Chan, N. Sai, R. Gearba, L. G. Kaake, K. J. Williams, K. Leung, P. J. Rossky, and X.-Y. Zhu, Hot charge-transfer excitons set the time limit for charge separation at donor/acceptor interfaces in organic photovoltaics, Nat. Mater. **12**, 66 (2013).

[4] T. Birol, N. A. Benedek, and C. J. Fennie, Interface Control of Emergent Ferroic Order in Ruddlesden-Popper Sr N + 1 Ti N O 3 N + 1, Phys. Rev. Lett. **107**, 257602 (2011).

[5] F. S. Bates and G. H. Fredrickson, Block copolymer thermodynamics: Theory and experiment, Annu. Rev. Phys. Chem. **41**, 525 (1990).

[6] C. Sinturel, F. S. Bates, and M. A. Hillmyer, High χ-low N block polymers: How far can we go?, ACS Macro Lett. **4**, 1044 (2015).

[7] T.-H. Chang, S. Xiong, R. M. Jacobberger, S. Mikael, H. S. Suh, C.-C. Liu, D. Geng, X. Wang, M. S. Arnold, Z. Ma, and P. F. Nealey, Directed self-assembly of block copolymer films on atomically thin graphene chemical patterns, Sci. Rep. **6**, 31407 (2016).

[8] K. Thorkelsson, P. Bai, and T. Xu, Self-assembly and applications of anisotropic nanomaterials: A review, Nano Today **10**, 48 (2015).

[9] J. Kao, K. Thorkelsson, P. Bai, Z. Zhang, C. Sun, and T. Xu, Rapid fabrication of hierarchically structured supramolecular nanocomposite thin films in one minute, Nat. Commun. **5**, 4053 (2014).

[10] C. H. Guo, Y. H. Lin, M. D. Witman, K. A. Smith, C. Wang, A. Hexemer, J. Strzalka, E. D. Gomez, and R. Verduzco, Conjugated block copolymer photovoltaics with near 3% efficiency through microphase separation, Nano Lett. **13**, 2957 (2013).

[11] C. Grieco, M. P. Aplan, A. Rimshaw, Y. Lee, T. P. Le, W. Zhang, Q. Wang, S. T. Milner, E. D. Gomez, and J. B. Asbury, Molecular rectification in conjugated block copolymer photovoltaics, J. Phys. Chem. C **120**, 6978 (2016).

[12] P. Perrin and R. E. Prud' homme, SAXS measurements of interfacial thickness in amorphous polymer blends containing a diblock copolymer, Macromolecules **27**, 1852 (1994).

[13] B. J. Reynolds, M. L. Ruegg, T. E. Mates, C. J. Radke, and N. P. Balsara, Experimental and theoretical study of the adsorption of a diblock copolymer to interfaces between two homopolymers, Macromolecules **38**, 3872 (2005).

[14] T. P. Russell, Changes in polystyrene and poly(methyl methacrylate) interactions with isotopic substitution, Macromolecules **26**, 5819 (1993).

[15] D. F. Sunday and R. J. Kline, Reducing block copolymer interfacial widths through polymer additives, Macromolecules **48**, 679 (2015).

[16] J. M. Virgili, Y. F. Tao, J. B. Kortright, N. P. Balsara, and R. A. Segalman, Analysis of order formation in block

copolymer thin films using resonant soft x-ray scattering, Macromolecules **40**, 2092 (2007).
[17] C. Wang, A. Garcia, H. P. Yan, K. E. Sohn, A. Hexemer, T. Q. Nguyen, G. C. Bazan, E. J. Kramer, and H. Ade, Interfacial widths of conjugated polymer bilayers, J. Am. Chem. Soc. **131**, 12538 (2009).
[18] G. E. Mitchell, B. G. Landes, J. Lyons, B. J. Kern, M. J. Devon, I. Koprinarov, E. M. Gullikson, and J. B. Kortright, Molecular bond selective x-ray scattering for nanoscale analysis of soft matter, Appl. Phys. Lett. **89**, 044101 (2006).
[19] B. A. Collins, Z. Li, J. R. Tumbleston, E. Gann, C. R. McNeill, and H. Ade, Absolute measurement of domain composition and nanoscale size distribution explains performance in PTB7:PC71BM solar cells, Adv. Energy Mater. **3**, 65 (2013).
[20] D. F. Sunday, M. R. Hammond, C. Wang, W. Wu, D. M. Delongchamp, M. Tjio, J. Y. Cheng, J. W. Pitera, and R. J. Kline, Determination of the internal morphology of nanostructures patterned by directed self-assembly, ACS Nano **8**, 8426 (2014).
[21] C. Wang, D. H. Lee, A. Hexemer, M. I. Kim, W. Zhao, H. Hasegawa, H. Ade, and T. P. Russell, Defining the nanostructured morphology of triblock copolymers using resonant soft x-ray scattering, Nano Lett. **11**, 3906 (2011).
[22] D. T. Wong, C. Wang, K. M. Beers, J. B. Kortright, and N. P. Balsara, Mesoporous block copolymer morphology studied by contrast-matched resonant soft x-ray scattering, Macromolecules **45**, 9188 (2012).
[23] S. Smadici, J. C. T. Lee, S. Wang, P. Abbamonte, G. Logvenov, A. Gozar, C. D. Cavellin, and I. Bozovic, Superconducting Transition at 38 K in Insulating-Overdoped La2CuO4-La1.64Sr0.36CuO4 Superlattices: Evidence for Interface Electronic Redistribution from Resonant Soft X-Ray Scattering, Phys. Rev. Lett. **102**, 107004 (2009).
[24] P. Abbamonte, A. Rusydi, S. Smadici, G. D. Gu, G. A. Sawatzky, and D. L. Feng, Spatially modulated "Mottness" in La2-xBaxCuO4, Nat. Phys. **1**, 155 (2005).
[25] B. A. Collins, Y. S. Chu, L. He, D. Haskel, and F. Tsui, Structural and chemical ordering of Heusler CoxMnyGez epitaxial films on Ge (111): Quantitative study using traditional and anomalous x-ray diffraction techniques, Phys. Rev. B **92**, 224108 (2015).
[26] B. A. Collins, J. E. Cochran, H. Yan, E. Gann, C. Hub, R. Fink, C. Wang, T. Schuettfort, C. R. McNeill, M. L. Chabinyc, and H. Ade, Polarized x-ray scattering reveals noncrystalline orientational ordering in organic films, Nat. Mater. **11**, 536 (2012).
[27] J. R. Tumbleston, B. A. Collins, L. Yang, A. C. Stuart, E. Gann, W. Ma, W. You, and H. Ade, The influence of molecular orientation on organic bulk heterojunction solar cells, Nat. Photonics **8**, 385 (2014).
[28] K. H. Stone and J. B. Kortright, Molecular anisotropy effects in carbon K-edge scattering: Depolarized diffuse scattering and optical anisotropy, Phys. Rev. B **90**, 104201 (2014).
[29] A. J. Allen, F. Zhang, R. J. Kline, W. F. Guthrie, and J. Ilavsky, NIST standard reference material 3600: Absolute intensity calibration standard for small-angle x-ray scattering, J. Appl. Crystallogr. **50**, 462 (2017).
[30] R.-J. J. Roe, Methods of X-Ray and Neutron Scattering in Polymer Science (Oxford University Press, New York, 2000).
[31] D. Tatchev, Multiphase approximation for small-angle scattering, J. Appl. Crystallogr. **43**, 8 (2010).
[32] See Supplemental Material at http://link.aps.org/supplemental/10.1103/PhysRevLett.119.167801 for specific sample preparation conditions, a table of basic sample parameters, sample transmission functions, absolute scattering calibration analysis, Qz scattering corrections, and all-sample fit results.
[33] H. Yan, C. Wang, A. R. McCarn, and H. Ade, Accurate and Facile Determination of the Index of Refraction of Organic Thin Films Near the Carbon 1s Absorption Edge, Phys. Rev. Lett. **110**, 177401 (2013).
[34] S. G. Urquhart, M. Martinson, S. Eger, V. Murcia, H. Ade, and B. A. Collins, Connecting Molecular Conformation to Aggregation in P3HT Using near Edge X-Ray Absorption Fine Structure Spectroscopy, J. Phys. Chem. C **121**, 21720 (2017).
[35] D. F. Sunday, E. P. Chan, S. V. Orski, R. C. Nieuwendaal, and C. M. Stafford, Evaluating the Network Structure of Desalination Nanomembranes via Functional Group Quantification with Soft X-Ray Reflectivity (to be published).
[36] E. Gann, A. T. Young, B. A. Collins, H. Yan, J. Nasiatka, H. A. Padmore, H. Ade, A. Hexemer, and C. Wang, Soft x-ray scattering facility at the Advanced Light Source with real-time data processing and analysis, Rev. Sci. Instrum. **83**, 045110 (2012).
[37] J. H. Hubbell, P. N. Trehan, N. Singh, B. Chand, D. Mehta, M. L. Garg, R. R. Garg, S. Singh, and S. Puri, A review, bibliography, and tabulation of K, L, and higher atomic shell x-ray fluorescence yields, J. Phys. Chem. Ref. Data **23**, 339 (1994).
[38] Y. H. Liu, J. B. Zhao, Z. K. Li, C. Mu, W. Ma, H. W. Hu, K. Jiang, H. R. Lin, H. Ade, and H. Yan, Aggregation and morphology control enables multiple cases of high-efficiency polymer solar cells, Nat. Commun. **5**, 1 (2014).
[39] J. H. Carpenter, A. Hunt, and H. Ade, Characterizing morphology in organic systems with resonant soft x-ray scattering, J. Electron Spectrosc. Relat. Phenom. **200**, 2 (2015).
[40] E. Gann, A. Watson, J. R. Tumbleston, J. Cochran, H. Yan, C. Wang, J. Seok, M. Chabinyc, and H. Ade, Topographic measurement of buried thin-film interfaces using a grazing resonant soft x-ray scattering technique, Phys. Rev. B **90**, 245421 (2014).
[41] A. Hexemer and P. Muller-Buschbaum, Advanced grazing-incidence techniques for modern soft-matter materials analysis, IUCrJ **2**, 106 (2015).
[42] B. L. Henke, E. M. Gullikson, and J. C. Davis, X-ray interactions: Photoabsorption, scattering, transmission, and reflection at $E = 50 - 30,000$ eV, $Z = 1$–92, At. Data Nucl. Data Tables **54**, 181 (1993).